Voxel-based finite element modelling of wood elements based on spatial density and geometry data using computed tomography

Hartig, J. U.; Bieberle, A.; Engmann, C.; Haller, P.;

Originally published:

January 2021

Wood Research and Technology - Holzforschung 75(2021)8, 742-753

DOI: https://doi.org/10.1515/hf-2020-0105

Voxel-based finite element modelling of wood elements based on spatial density and geometry data using computed tomography

Jens U. Hartig[1*], André Bieberle[2], Chris Engmann[3], Peer Haller[1]

[1]Technische Universität Dresden, School of Civil and Environmental Engineering, Faculty of Civil Engineering, Institute of Steel and Timber Construction, 01062 Dresden, Germany

[2]Helmholtz-Zentrum Dresden-Rossendorf, Bautzner Landstraße 400, 01328 Dresden

[3]Alumnus Technische Universität Dresden

[*]Corresponding author: E-Mail: jens.hartig@tu-dresden.de, Tel.: +49-351-463-35784, Fax: +49-351-463-36306

Abstract:

In this paper, voxel-based finite element modelling based on spatial geometry and density data is applied to simulate the detailed stress and strain distribution in a large wooden element. As example, a moulded wooden tube with a length of 3 m and a diameter of 0.3 m is examined. Gamma-ray computed tomography is used to obtain the spatial distribution of elastic properties based on the correlation with density. Correlation functions between density and elastic material properties are experimentally determined and serve as link for defining the non-uniform distribution of the material properties in the finite element model. Moreover, also the geometry is obtained by the computed tomography. Due to the consideration of both the geometric imperfections and the spatial variation of the material properties, a detailed analysis of the stress and strain distribution of the wood element is performed. Additionally, a non-destructive axial compression test is performed on the wooden tube to analyse the load-bearing

behaviour. By means of digital image correlation, the deformation of the surface is obtained, which also serves for validation of the finite element model.

1 Introduction

The material properties of wood are non-uniformly distributed within a certain volume (Kollmann et al. 1968). Usually, this fact is ignored when wooden structures are modelled, e.g. with the finite element method (FEM). While the anisotropy in the mechanical behaviour is usually taken into account in such models at least to some extent, the spatial variation in the mechanical properties is typically neglected and a uniform distribution is assumed. A reason is that the spatial distribution of the values of the mechanical properties is usually not known for a wooden structure because it is virtually impossible to measure it directly. However, it is well known that there is a correlation between the density and mechanical properties like Young's modulus and strength (Kollmann et al. 1968). Thus, by means of the spatial distribution of the density in the wooden structure also the spatial distribution in the mechanical properties can be considered.

Computed tomography (CT) allows for the qualitative determination of the spatial density distribution in a specimen (Kak et al. 1988) and by means of a calibration with a homogeneous object of known density also quantitative information can be gathered (Schubert et al. 2011). Determination of density in wooden objects on the centimetre scale by means of CT is state of the art. At this scale, it is possible, e.g., to distinguish the spatial annual ring structure (Macedo et al. 2002, Wei et al. 2011). With micro-CT it is even possible to investigate the cell structure of the wood (Forsberg et al. 2008 and 2010). Investigations of large wood or timber structures, e.g. for building purposes, on the metre scale are, however, rare. A study by (Onoe et al. 1984) showed the

potential of CT for inspecting living trees. A recent study by (Pernkopf et al. 2019) evaluated the potential gain for sawmills using information from CT scanning of entire logs.

The spatial data of geometry and density determined by CT can be directly applied to generate a FEM model. Therefore, the so-called voxel-based meshing approach can be used, which uses a regular mesh of brick elements. The nodes of the elements correspond to the voxels in the CT data (Keyak et al. 1990, Lengsfeld et al. 1998). While this approach is common in medical simulations, e.g. for modelling of bones, it is not found in literature for wooden structures. Nevertheless, with such a detailed model incorporating both geometric imperfections and spatial variations of the material properties, the load-bearing behaviour of the structural element can be realistically described. Compared to common modelling approaches neglecting the spatial variations, more accurate results can be expected. The higher accuracy can result in engineering applications for instance to a more economic use of material since the uncertainty is substantially reduced and lower safety factors are necessary. For historical wooden structures, e. g. old timber buildings and other cultural heritage of wood, it would be also a way to evaluate, e. g., the serviceability of potentially damaged members or hygro-mechanical deformations (e. g. Konopka et al. 2019).

Wood can be modified for improving its properties. Novel structural elements of timber for technical applications have, e.g., a hollow profile in order to utilize the material efficiently. These elements can be produced in thermo-hygro-mechanical processes incorporating a densification transverse to the grain (Sandberg et al. 2013). The technique is called wood moulding (Haller 2007, Kutnar et al. 2015). The densification is another source of density variations in the structural element. A moulded wooden tube (MWT) (Hartig et al. 2016) was used as an example of application for the voxel-based simulation approach.

In the current investigations, the MWT specimen has a length of 3 m and a diameter of 0.3 m and was initially investigated by gamma-ray CT. Subsequently, the specimen was tested under

compression parallel to the grain while the deformation on the surface was measured by digital image correlation (DIC). DIC allows for the spatial measurement of deformations on the surface of the specimen (Zink et al. 1995). The measured deformations were used for the validation of the results of FEM simulations, which consider spatial variations in the mechanical properties and geometrical imperfections.

2 Material and methods

2.1 Wood moulding

Wood moulding is a thermo-hygro-mechanical process to deform wood in a plastic manner without destroying the cell structure. It is used to produce structural elements, like tubes, with low loss of material during the processing and high structural efficiency due to the technical profile. Wood moulding is described in the literature (Haller 2007, Kutnar et al. 2015, Hartig et al. 2016). Thus, only a short summary is given here. For producing moulded wood, the following steps are mainly necessary:

- Densification of ordinary sawn wood transverse to the grain at a temperature above 80°C to soften the lignin
- Cooling of the densified wood to ambient temperature to fix the densification by re-hardening of the lignin
- Cutting of the densified wood into pieces according to the wall thickness of the structural element
- Glue-lamination of the cut pieces to a board such that the densification is oriented in the plane of the board
- Steam treatment of the board at a temperature of about 100°C in order to re-soften the lignin

- Shaping of the soft board by pressing it into a moulding tool where the moulded wood is cooling down to ambient temperature to fix the shape
- Optionally, a subsequent fixation process, e.g., by hot-steam treatment can be applied to increase the dimensional stability of the moulded wood under moisture variations in service

The wood moulding process changes the original density distribution in several ways. The density is already non-uniformly distributed in clear wood due to e.g. annual rings and differences in growth due to annually changing climatic conditions but also due to aging processes within a tree. The densification step increases and homogenises the density compared to the clear wood, provided that appropriate process parameters are applied. Steam treatment leads to a relatively uniform decrease of the density due to the recovery by the shape memory effect. In the shaping step, a density gradient is induced over the wall thickness due to the non-uniform bending deformation leading to a reduction of density towards the convex surface.

For the evaluation of experimentally obtained results, the theoretical value of density change due to the moulding process is interesting to know. In (Hartig et al. 2016), equations for determining the strain distribution due to the moulding are set up. The strain on the inner surface ε_i is calculated as

$$\varepsilon_i = \frac{2r_i\varepsilon_{str} - w_b}{2r_i + w_b} \tag{1}$$

and the strain on the outer surface ε_o as

$$\varepsilon_o = \frac{2r_o\varepsilon_{str} + w_b}{2r_o - w_b} \tag{2}$$

where w_b, r_i and r_o are wall thickness, inner and outer radius of the moulded element, and ε_{str} is a uniform strain across w_b, e.g. due to swelling or stretching. The initial density ρ_{ini} of a cubic element is calculated with

$$\rho_{ini} = \frac{m}{whl} \tag{3}$$

where *m*, *w*, *h*, *l* are mass, width, height and length. Assuming only Δl is changed due to the forming results in a density after recovery ρ_{rec} of

$$\rho_{rec} = \frac{m}{wh(l+\Delta l)} = \frac{m}{whl(1+\varepsilon)} = \frac{\rho}{(1+\varepsilon)} \text{ with } \varepsilon = \frac{\Delta l}{l}. \tag{4}$$

Inserting Eq. (1) and Eq. (2) in Eq. (4), respectively, results in the density on the outer and inner surface $\rho_{rec,o}$ and $\rho_{rec,i}$ after forming/recovery

$$\rho_{rec,o} = \frac{\rho_{ini}}{\left(1+\frac{2r_o\varepsilon_{str}+w_b}{2r_o-w_b}\right)} \tag{5}$$

and

$$\rho_{rec,i} = \frac{\rho_{ini}}{\left(1+\frac{2r_i\varepsilon_{str}-w_b}{2r_i+w_b}\right)} = \frac{\rho_{ini}}{\left(1+\frac{2(r_o-w_b)\varepsilon_{str}-w_b}{2r_o-w_b}\right)} \text{ with } r_i = r_o - w_b. \tag{6}$$

The difference between the density on the outer and inner surface of the tube is then calculated with

$$\Delta\rho_{io} = \rho_{rec,i} - \rho_{rec,o} = \frac{\rho_{ini}w_b(2r_o-w_b)}{2r_o(r_o-w_b)(1+\varepsilon_{str})}. \tag{7}$$

2.2 Determination of spatial density distribution

The spatial density distribution of the MWT is non-invasively investigated in different cross-sections *x*,*y* along the entire tube length *z* using gamma-ray computed tomography (CT) as introduced by Hampel et al. (2007). This CT scanner is primarily designed for investigations on gas-liquid two-phase flow in technical devices (Tschentscher et al. 2011, Härting et al. 2015, Bieberle et al. 2015, Neumann et al. 2016, Rollbusch et al. 2015, Groß et al. 2019) but can also be used for non-destructive testing purposes. As radiation source ^{137}Cs is used with an activity of

180 GBq and a photon energy line of 662 keV. With that, walls of high density can be penetrated and a good phase contrast is achieved.

The radiation detector contains N_d=320 single scintillation detectors that measure gamma photons passing the MWT without interaction. The radiation is attenuated according to Beer-Lamberts law

$$N_x = N_0 \cdot \mathrm{e}^{-\sum_i \mu_i \cdot d_i} \tag{8}$$

where N_0 is the radiation intensity without object, μ is the attenuation coefficient, d is the interaction length of the material and i is referred to each material the ray is passed. Thus, the attenuation signal at each single detector E_d is calculated as

$$E_d = \ln\frac{N_0}{N_x} = \sum_i \mu_i \cdot d_i \tag{9}$$

By rotating the source-detector ensemble around the moulded wooden tube, such attenuation projections are acquired from different angular positions p (see Figure 1a). The obtained data matrix $E_{d,p}$ is finally used as input for computed tomography reconstruction algorithms (Kak et al. 1988) to achieve non-superimposed cross-sectional attenuation coefficient distributions $\mu_{i,j}$, i.e. slice images of the tube, with i and j as two-dimensional image index.

The CT scanner is able to perform CT scans at several heights of the tube of maximal 1700 mm. Thus, the 3 m long moulded wooden tube is initially scanned from the bottom to the middle, then horizontally turned and finally scanned from the middle to the top. The distance between each CT scan is 0.05 m (see Figure 1b). For a CT scan, 1000 projections are equidistantly acquired for an interval of approx. 10 min. To obtain slice images, simultaneous iterative reconstruction technique (SIRT) is applied on a reconstruction image pixel grid $i \times j$ of 0.5 × 0.5 mm² pixel size using the open source tools ASTRA (Aarle et al. 2015, Aarle et al. 2016, Palenstijn et al. 2011) and OCTAVE v4.2.1 on a graphic processing unit (GPU).

In a last data processing step, the reconstructed attenuation coefficients $\mu_{i,j}$ are normalized to density values $\rho_{i,j}$ using a reference probe 'ref'. In our case, a tube of tapped water is additionally placed in one of all CT scanning planes. The subsequently determined $\bar{\mu}_{ref}$ and their known density ρ_{ref} are then used to calculate the density values of the reconstructed slice images

$$\rho_{i,j} = \frac{\mu_{i,j}}{\bar{\mu}_{\mathrm{ref}}} \cdot \rho_{\mathrm{ref}}. \tag{10}$$

Eventually, the determined deviation of μ_{ref} is measured to be ±2% and defines, hence, the measuring deviation of the determined wood density values.

2.3 Mechanical testing of the MWT

A compression test is performed on the MWT in a standard mechanical testing machine where the load is applied with displacement control as described in (Heiduschke et al. 2010, Hartig et al. 2016). The MWT is tested non-destructively in order to be able to extract samples for the determination of material properties afterwards (see section 2.4). The pressing plates are fixed after a negligible preloading. The applied force F is measured with a load cell. Digital image correlation (DIC) is used to determine the deformation on the surface of the specimen. In DIC, the displacement field of a randomly distributed speckle pattern is recorded by a camera system on several load levels. At least two cameras, which have to observe the same surface from two different positions, are necessary for determining spatial deformations. Based on the data obtained, the strain distribution on the surface can be calculated (e.g. Luo et al. 1993, Sutton et al. 2008). The commercially available DIC system VIC-3D (version 8) by CORRELATED SOLUTIONS is used.

2.4 Mechanical testing of material samples

The elastic properties of wood, i.e., Young's moduli, shear moduli and Poisson's ratios correlate with the density to a different extent (Kollmann et al. 1968). As literature on the correlation between density and mechanical properties is rather rare, especially for densified beech, tests for the

current analysis are performed with specimens obtained from the MWT tested non-destructively under compression as described in Section 2.3. Since the available number of specimens is limited with this approach, only the correlation of Young's moduli E_l and E_t in longitudinal and transverse direction is determined experimentally. For the shear moduli and Poisson's ratios, constant values are assumed. At least for the shear moduli, this assumption is supported by experimental results by (Kollmann et al. 1960).

For determining the Young's modulus in longitudinal direction E_l, compression tests are performed and for the Young's modulus in transverse direction E_0 tension tests. The cross sectional area of the specimens was limited by the wall thickness of 20 mm and the curved shape of the wall of the tube. It shall be also noted that the density varied over the cross section; as shown subsequently in Figure 3. In total, about 30 tests were performed for each, E_l and E_t. The respective test setups are illustrated inside the diagrams in Figure 5. The force F was measured with a load cell and the deformation Δu with linear variable displacement transducers (LVDT). Based on F and Δu, the Young's moduli E_0 and E_{90} were determined corresponding to (EN 408). The specimens were tested at ambient temperature and had a moisture content of 8-10 %.

2.5 Finite Element Method (FEM)

The density and geometry data obtained from the CT scan is used to create a finite element model. Therefore, the standard finite element software ABAQUS is applied. Linear volume elements with eight nodes (C3D8) are created such that 2 by 2 nodes/pixels in two subsequent slice images of the CT reconstruction form an element. However, an element is only created if the density at all the eight pixels is above a threshold value of 600 kg m^{-3} corresponding to the assumed minimum density of untreated beech. If the density at the pixel is lower, the respective volume is considered as void. This method is also called voxel-based meshing (e.g. Keyak et al. 1990, Lengsfeld et al. 1998).

Corresponding to the spatial resolution of the reconstructed slice image, across the wall thickness about 40 elements and in longitudinal direction about 60 elements exist corresponding to the number of slices. In total, the model consists of about 3.8 million elements, 4.1 million nodes and 12.2 million degrees of freedom. A transverse isotropic material law is applied, which needs six coefficients for the complete description:

- E_l – Young's modulus in longitudinal direction
- E_t – Young's modulus in transverse direction
- G_{lt} – Shear modulus between longitudinal and transverse direction
- G_{tt} – Shear modulus for rolling shear
- ν_{lt} – Poisson's ratio between longitudinal and transverse direction
- ν_{tt} – Poisson's ratio within transverse direction

The longitudinal material direction is aligned parallel to the axial direction of the MWT and the transverse direction is placed perpendicular. The elastic material properties are defined for each element proportional to the density at this position determined by CT. More information about the assumed correlations between the density and the elastic properties is given in Section 3.4.

The load is applied as prescribed displacement of 10 mm on one of the end cross-sectional areas in axial direction of the tube. The remaining degrees of freedom at the two cross-sectional areas at the end of the tube were assumed equal to zero corresponding to the restricted deformation at the loading plates due to friction. A linear-elastic simulation was carried out.

3 Results and discussion

3.1 Object of investigation

The analysis was performed on a MWT made of beech (*Fagus sylvatica* L.), with an average outer diameter of 0.3 m, a wall thickness of 0.02 m and a length of 3.0 m. In (Hartig et al. 2016) more

information about the production of the MWT and the mechanical properties is given. The wood possessed a moisture content of about 9%. The tests were carried out at ambient temperature without special climatic conditioning.

Using Eq. (7), the density difference between the inner and outer surface is estimated. With $r_o \approx 0.16$ mm, $w_b \approx 0.020$ m, $\varepsilon_{str} \approx 0.1$ and $\rho_{ini} \approx 1000$ kg m^{-3}, Eq. (7) results in a theoretical density difference between the inner and outer surface of $\Delta\rho_{io} = 122$ kg m^{-3}. With $\varepsilon_{str} = 0$, it results $\Delta\rho_{io} = 134$ kg m^{-3}, which reveals a minor influence of ε_{str}.

3.2 Density distribution

The density distribution in the MWT was determined by CT as described in Section 2.2. The resolution of the CT scanner of 2 mm results at the pixels at the surface of the tube to erroneous results since the density of the air, which is approximately zero, and the density of the wood are mixed at this area. It can be estimated that at least a 2 mm region at the surface is strongly affected. Since the tube has a thickness of about 20 mm, only 16 mm or 80% of the tube are available for evaluation. This effect is, supposedly, negligible for compact specimens, but has significant influence for thin-walled specimens like the MWT.

Figure 2 and Figure 3 show the density distribution in the tube. The subdivision by the glued joints is clearly observable due to the lower density at these positions (Figure 3a). Moreover, it can be also seen that the highest density is in many cases located in the middle of the wood segments, which means that there was either a higher compression or less recovery than in the parts in the vicinity of the glued joints. Highly densified regions tend to a worse deformability as already observed in (Hartig et al. 2016) and can be explained by a hornification of the material (Fernandes Diniz et al. 2004). In circumferential direction, it is observable that there are some segments, which have considerably higher density.

The density distribution in circumferential direction is evaluated more thoroughly. In Figure 3, it can exemplarily be seen for a representative slice in the centre of the tube that, as expected, the density on the outer surface is smaller than on the inner surface. The difference is also shown in Figure 3b. The mean value of the difference corresponding to $\Delta\rho_{io}$ is 102 kg m^{-3}, which corresponds well with the theoretical value of 122 kg m^{-3} according to Eq. (7) as calculated in Section 3.1. It shall be noted that due to the expected inaccurateness of the density values of the boundary pixels only a thickness portion of 15 mm was taken into account. Thus, the density difference for the 20 mm will correspond even better to the theoretical value.

3.3 Load-bearing behaviour of the MWT

The load-bearing behaviour of the MWT was determined in a compression test as described in Section 2.3. The maximum applied load was 900 kN, which corresponds to approximately 75% of the ultimate load of about 1200 kN as determined in destructive testing in (Hartig et al. 2016). The force-deformation relation, Figure 6, shows at the beginning setting due to imperfections in the evenness of the load areas. Afterwards, linear elastic behaviour is observable.

Figure 4 shows the strain distribution on the surface determined with DIC. In longitudinal direction, the strain ε_l, which is on the entire measurement surface in the compressive range, is non-uniformly distributed due to the heterogeneity of the material as well as geometric imperfections of the tube. The distribution of ε_l shows distinct concentrations at the ends of the tube due to deformation constraints of the supports. In transverse direction, the strain ε_t is also non-uniformly distributed but stronger than in axial direction. On most of the measurement surface, the strains are in the tensile range but there exist also clusters in the compressive range. The observation of heterogeneity in the strain distribution transverse and parallel to the loading direction is in accordance with results of wood compression tests presented by (Zink et al. 1995).

3.4 Correlation between density and mechanical properties

For determining correlation functions for the density ρ with the Young's moduli E_l and E_t, experiments according to Section 2.4 were performed. Figure 5 shows the determined Young's moduli depending on the density of the samples. For E_l, a linear regression function starting at the point of origin was assumed as correlation function, see Figure 5a. For E_t, an exponential regression function was assumed to take into account the progressively increasing modulus with increasing density, see Figure 5b. It is worth to note that undensified beech has a Young's modulus transverse to the grain in the range of $E_t \approx 1000$ MPa, which is approximately one order of magnitude more than the densified material of the same density (≈ 700kg/m³). It can be explained by buckling of the cell walls during the densification process. Thus, the exponential regression function might be only applied for densified wood. In summary, the six elastic properties of the transverse isotropic material law were defined as following:

- $E_l = 21\ \rho$ (for E_l in MPa and ρ in kg m^{-3})
- $E_t = 16 \exp(0.0032\ \rho)$ (for E_t in MPa and ρ in kg m^{-3})
- $G_{lt} = 1200$ MPa*
- $G_{tt} = 400$ MPa*
- $\nu_{lt} = 0.04$ MPa*
- $\nu_{tt} = 0.46$ MPa*

(*based on (Ozyhar et al. 2012) for undensified beech)

3.5 FEM simulation

The compression test as described in Section 3.3 was simulated with a FE model as described in Section 2.4. The global load-bearing behaviour is well reproduced by the model as the force-

deformation relation in Figure 6 shows. While the setting at the beginning of loading cannot be reproduced in the linear-elastic simulation, the slope of force-deformation relation corresponding to the axial stiffness of the MWT coincides well. As to be expected, the axial stiffness in the simulation is slightly lower in the model since the regions at the surface are not taken into account and, thus, the wall thickness is less than in the experiment.

The strain distribution as determined by DIC, see Figure 4, is also used for validation of the model. It is compared to the strain distribution as determined in the simulation and shown in Figure 7. The strain in transverse direction shows a similar distribution in experiment and simulation. The zone of low strain in the mid-section of the tube changing the direction diagonally can be identified in both simulation and experiment. The strain distribution in longitudinal direction (Figure 7a) shows for simulation and experiment a more uniform distribution although there are also strain concentrations observable – more pronounced in the experimental data. In both simulation and experiment, the strain in the centre part is smaller than at the ends, which can be explained by the higher Young's modulus in the centre part as indicated already in the density distribution in Figure 2.

Although there is no perfect agreement between simulation and experiment, the validity of the model can be confirmed. There are several properties of the model, which prevent a better agreement. One reason is that the resolutions of the FEM mesh and the DIC approximation are different. Moreover, there are several sources of uncertainty regarding the finite element model, e.g. the correlation between density and elastic properties as well as the real conditions of load application. In addition, the reduced cross section resulting from the resolution deficiency of the CT at the surface as already mentioned before is a reason of the disagreement. Certainly, also the assumption of a transverse isotropic material behaviour has an influence since the elastic behaviour of wood is different in radial and tangential direction. This effect cannot be taken into account with

the given data for the densified wood. However, for untreated wood it might be considered with reasonable effort.

Besides the strain distribution, the model allows also to investigate the stress distribution, which is experimentally inaccessible. Figure 8 shows the calculated stress distribution. It can be seen that the stresses do not directly correlate with the strains although a linear-elastic material law is applied. In longitudinal direction, the maximum stress on the shown surface is approximately 60 MPa (Figure 8a). This corresponds approximately to the strength of clear wood. The longitudinal stress is larger on the inner surface due to the higher Young's modulus. The maximum stress in the entire tube is about 90 MPa. The maxima are located in the centre region of the wood segments as it can be seen in Figure 8b where is often also the highest density situated. In transverse direction, the stresses are considerably lower than in longitudinal direction (Figure 8c,d). The maximum value in the observable range is about 0.25 MPa. The maximum tensile stress in entire tube is about 0.5 MPa, which is about one order of magnitude smaller than the strength in transverse direction.

Moreover, the model allows also for an estimation of the influence of the spatially non-uniform distribution of the material properties on the load-bearing behaviour. Therefore, a model with a uniform distribution of the material properties is used. The Young's modulus in longitudinal direction was defined as E_l = 17000 MPa, which results approximately in the same reaction force in longitudinal direction corresponding to Figure 6, und in transverse direction as E_t = 400 MPa. The strain distribution is shown in Figure 9. The strains are more uniformly distributed and the extreme values have a smaller magnitude than in the simulation with non-uniformly distributed elastic properties. Nevertheless, concentrations due to geometrical imperfections are still present. The gap is the influence of the non-uniform elastic properties. The stresses have, as shown in Figure 10, also a more uniform distribution. Therefore, the segments of the tube can also not to be identified as it was the case in the simulation with non-uniformly distributed elastic properties.

4 Conclusions

In this paper, an enhanced approach for FEM modelling of wooden structures based on voxel-based meshing using geometry and density information by CT was investigated. It was shown that computed tomography is well-suited for determining density variations in timber structural elements and it can be also used to determine accurately the geometrical shape of wood and timber elements. By applying correlation functions, also variations in mechanical properties due to varying density can be directly taken into account in the finite element model. With this modelling approach, a very detailed FE analysis was performed, which gave insights in the spatial strain and stress distribution in the investigated sample. While the spatial strain distribution is also measurable experimentally, the spatial stress distribution can only be determined by simulation. The simulation shows that the results are not straightforward in the sense that the qualitative strain distribution corresponds directly to the stress distribution. This results from several sources: the anisotropy of the material, the imperfect geometry and the non-uniform distribution of the elastic properties. The effect of the non-uniform distribution of the elastic properties can and was quantified by the comparison with the simulation assuming uniform elastic properties. The behaviour will become even more complex when inelastic material behaviour is taken into account, which could be a next step of investigation. It shall be noted that due to the large number of degrees of freedom, the simulation took several hours on a standard personal computer. Thus, for nonlinear simulations supercomputers need to be employed in order to obtain results in a reasonable time.

References

Bieberle, A., Schlottke, J., Spies, A., Schultheiss, G., Banzhaf, M., Kuehnel, W., Hampel, U. (2015) Hydrodynamics analysis in micro-channels of a viscous coupling using gamma-ray computed tomography, Flow Meas. Instr. 45:288-297

DIN 68364 (2003) Properties of wood species - Density, modulus of elasticity and strength

EN 408 (2012) Timber structures - Structural timber and glued laminated timber - Determination of some physical and mechanical properties

Fernandes Diniz, J.M.B., Gil, M.H., Castro, J.A.A.M. (2004) Hornification – its origin and interpretation in wood pulps. Wood Sci. Technol. 37:489–494

Groß, K., Bieberle, A., Gladyszewski, K., Schubert, M., Hampel, U., Skiborowski, M., Gorak A. (2019) Analysis of Flow Patterns in High-Gravity Equipment Using Gamma-Ray Computed Tomography. Chemie Ingenieur Technik 91:1032-1040

Haller, P. (2007) Concepts for textile reinforcements for timber structures. Mater. Struct. 40:107-118

Hampel, U., Bieberle, A., Hoppe, D., Kronenberg, J., Schleicher, E., Sühnel, T., Zimmermann, F., Zippe, C. (2007) High resolution gamma ray tomography scanner for flow measurement and non-destructive testing applications. Rev. Sci. Instrum. 78:103704.

Härting, H.-U., Bieberle, A., Lange, R., Larachi, F., Schubert, M. (2015) Hydrodynamics of co-current two-phase flow in an inclined rotating tubular fixed bed reactor - Wetting intermittency via periodic catalyst immersion, Chem. Eng. Sci. 28:147-158

Hartig, J.U., Wehsener, J., Haller, P. (2016) Experimental and theoretical investigations on moulded wooden tubes made of beech (*Fagus sylvatica* L.). Constr. Build. Mater. 126:527-536.

Heiduschke, A., Haller, P. (2010) Fiber-reinforced plastic-confined wood profiles under axial compression. Struct. Eng. Int. 20:246–253.

Kak, C., Slaney, M., Principles of Computerized Tomographic Imaging, IEEE Press, New York, 1988.

Keyak, J.H., Meagher, J.M., Skinner, H.B., Mote, C.D. (1990) Automated three-dimensional finite element modelling of bone: a new method. J. Biomed. Eng. 12:389-397

Kollmann, F.F.P., Côté, Jr. J.W. Principles of Wood Science and Technology - Part I: Solid Wood. Springer-Verlag, Berlin, 1968.

Kollmann, F., Krech, H. (1960) Dynamische Messung der elastischen Holzeigenschaften und der Dämpfung Ein Beitrag zur zerstörungsfreien Werkstoffprüfung. Holz als Roh- und Werkstoff. 18:41-54

Konopka, D., Ehricht, S., Kaliske, M. (2019) Hygro-mechanical investigations of clavichord replica at cyclic climate load: Experiments and simulations. J. Cult. Herit. 36:210-221

Kutnar, A., Sandberg, D., Haller, P. (2015) Compressed and moulded wood from processing to products – a review. Holzforschung. 69:885-897

Lengsfeld, M., Schmitt, J., Alter, P., Kaminsky, J., Leppek, R. (1998) Comparison of geometry-based and CT voxel-based finite element modelling and experimental validation Med. Eng. Phys. 20:515-522

Luo, P.F., Chao, Y.J., Sutton, M.A., Peters, III W.H. (1993) Accurate measurement of three-dimensional deformations in deformable and rigid bodies using computer vision. Exp. Mech. 33:123-132

Macedo, A., Vaz, C., Pereira, J., Naime, J., Cruvinel, P., Crestana, S. (2002) Wood Density Determination by X- and Gamma-Ray Tomography. Holzforschung, 56:535-540

Neumann, M., Schäfer, T., Bieberle, A., Hampel, U. (2016) An Experimental Study on the Gas Entrainment in Horizontally and Vertically Installed Centrifugal Pumps, J. Fluids Eng. 138(9): 091301 (9 pages)

Onoe, M., Tsao, J., Yamada, H., Nakamura, H., Kogure, J., Kawamura, H., Yoshimatsu, M. (1984) Computed tomography for measuring the annual rings of a live tree. Nucl. Instrum. Methods Phys. Res. 221:213-220

Ozyhar, T., Hering, S. Niemz, P. (2012) Moisture-dependent elastic and strength anisotropy of European beech wood in tension, J. Mater. Sci. 47:6141–6150

Pernkopf, M., Riegler, M., Gronalt, M. (2019) Profitability gain expectations for computed tomography of sawn logs. Eur. J. Wood Wood Prod. 77:619-631

Rollbusch, P.; Becker, M.; Ludwig, M.; Bieberle, A.; Grünewald, M.; Hampel, U.; Franke, R. (2015) Experimental investigation of the influence of column scale, gas density and liquid properties on gas holdup in bubble columns, Int J Multiphase Flow 75: 88-106

Sandberg, D., Haller, P., Navi, P. (2013) Thermo-hydro and thermo-hydro-mechanical wood processing: An opportunity for future environmentally friendly wood products. Wood Mater. Sci. Eng. 8:1-25

Schubert, M., Bieberle, A., Barthel, F., Boden, S., Hampel, U. (2011) Advanced tomographic techniques for flow imaging in columns with flow distribution packings, Chemie Ingenieur Technik 83: 979-991

Sutton, M.A., Yan, J.H., Tiwari, V., Schreier, H.W., Orteu, J.J. (2008) The effect of out-of-plane motion on 2D and 3D digital image correlation measurements. Opt. Lasers Eng. 46:746-757

Tschentscher, R., Schubert, M., Bieberle, A., Nijhuis, T.A., van der Schaaf, J., Hampel, U., Schouten, J.C. (2011) Tomography measurements of gas holdup in rotating foam reactors with Newtonian, non-Newtonian and foaming liquids, Chem. Eng. Sci. 66:3317–3327

Visscher, F., Bieberle, A., Schubert, M., van der Schaaf, J., de Croon, M., Hampel, U., Schouten, J. (2012) Water and n-heptane volume fractions in a rotor-stator spinning disc reactor, Ind. Eng. Chem. Res. 51: 16670-16676

Wei, Q., Leblon, B., La Rocque, A. (2011) On the use of X-ray computed tomography for determining wood properties: a review. Can. J. For. Res. 41:2120-2140.

van Aarle, W. , Palenstijn, W. J., Cant, J., Janssens, E., Bleichrodt, F., Dabravolski, A., De Beenhouwer, J., Batenburg, K. J., Sijbers, J. (2016) Fast and Flexible X-ray Tomography Using the ASTRA Toolbox, Opt. Express 24: 25129-25147

van Aarle, W., Palenstijn, W. J., De Beenhouwer, J., Altantzis, T., Bals, S., Batenburg, K. J., Sijbers, J. (2015) The ASTRA Toolbox: A platform for advanced algorithm development in electron tomography, Ultramicroscopy 157:35–47

Palenstijn, W. J., Batenburg, K. J., Sijbers, J. (2011) Performance improvements for iterative electron tomography reconstruction using graphics processing units (GPUs), J. Struct. Biol. 176:250-253

Zink, A.G., Davidson, R.W., Hanna, R.B (1995) Strain Measurement in Wood using A Digital Image Correlation Technique, Wood and Fiber Sci. 27:346-359

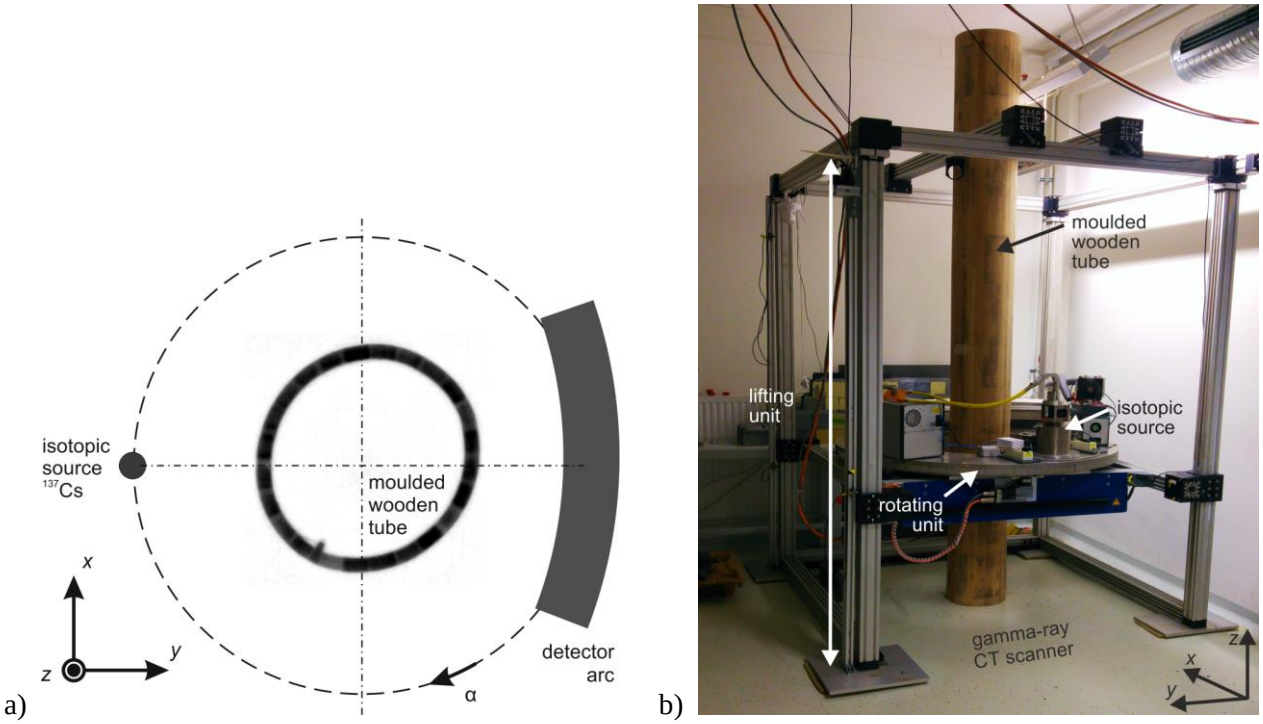

Figure 1: Setup for gamma-ray computed tomography; a) sketch of measurement principle, b) setup of gamma-ray CT applied to the MWT.

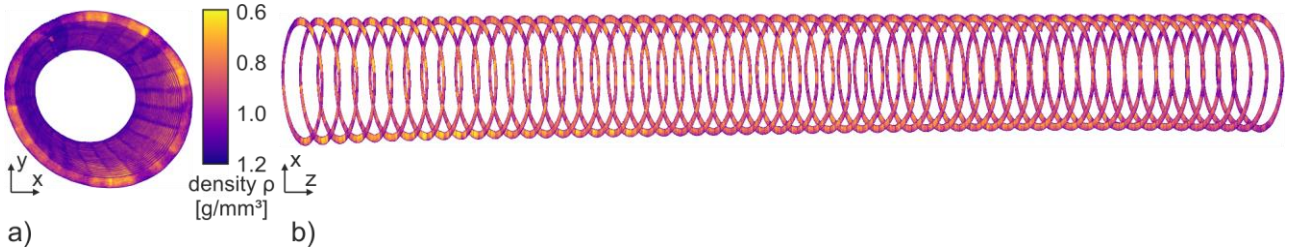

Figure 2: Density distribution of the moulded wood tube visualised by image stacks; a) three-dimensional view into the tube, b) three-dimensional outside the tube from bottom (left side) to the top (right side).

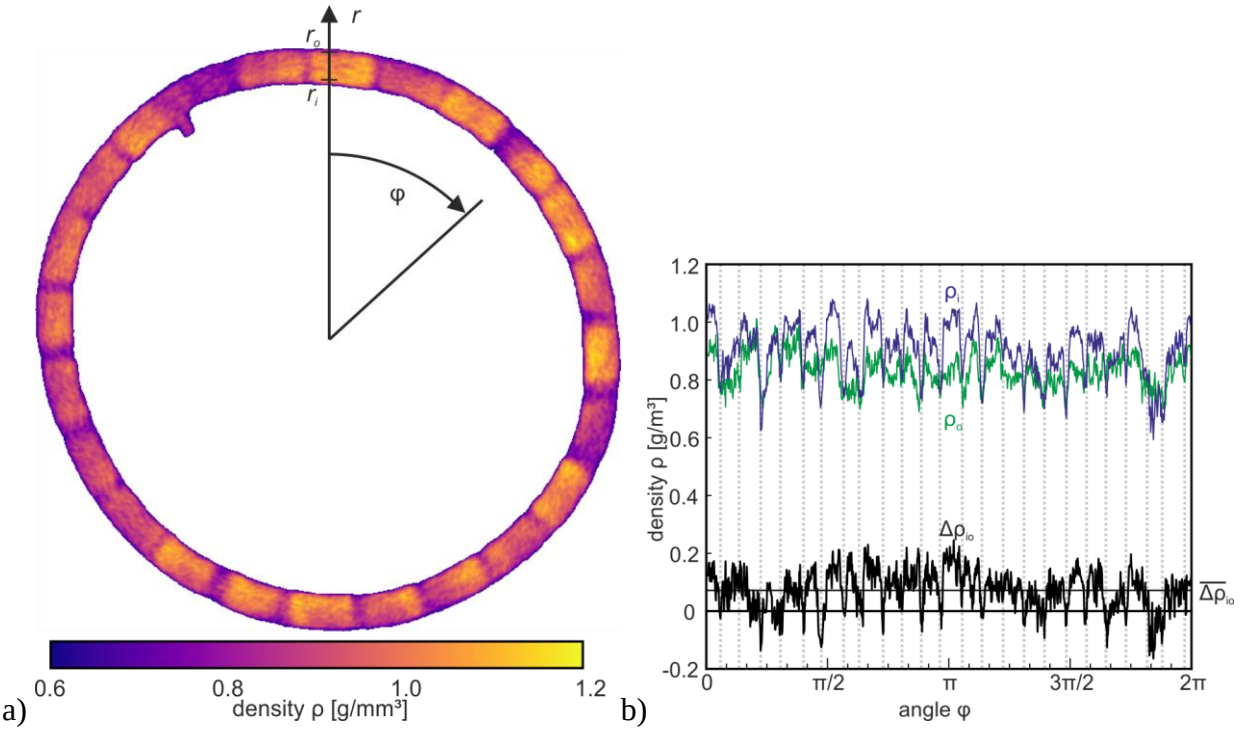

Figure 3: Evaluation of density distribution in a representative CT scanning plane; a) visualisation of density in cross section, b) corresponding radial density values.

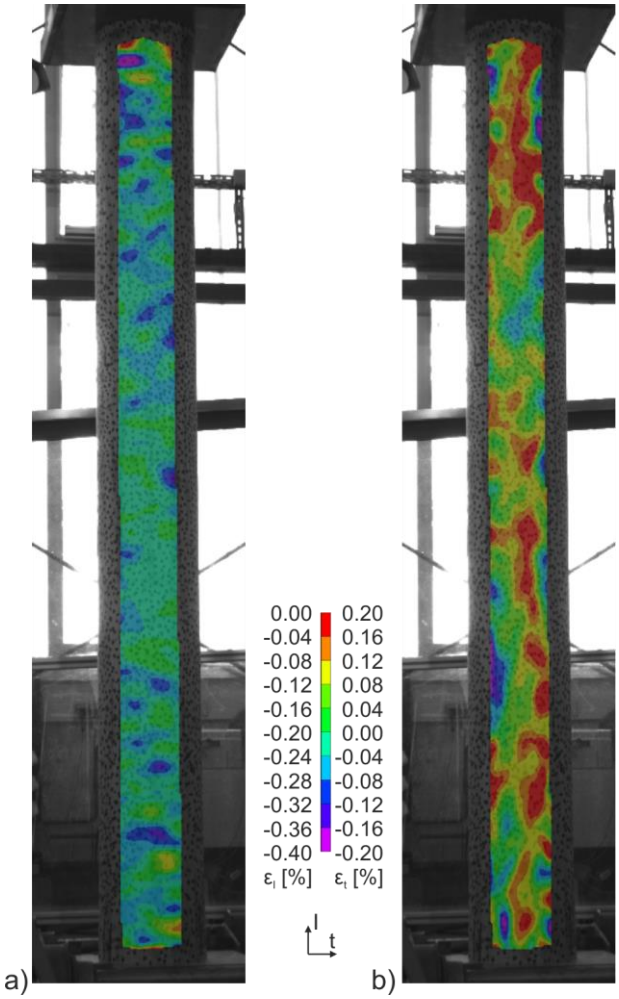

Figure 4: Strain distributions on the surface of the tube; a) strain in longitudinal direction ε_l, b) strain in transverse direction ε_t

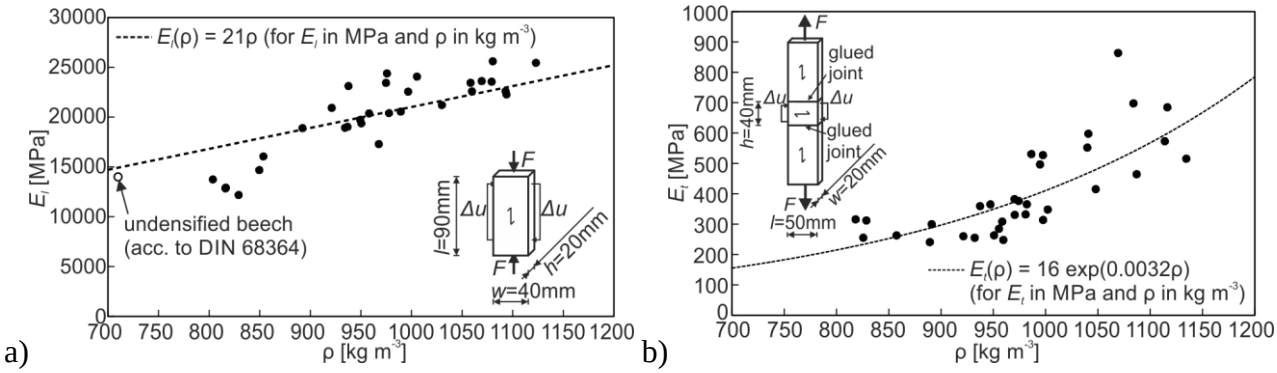

Figure 5: Results of the material tests for determining the Young's moduli; a) E_l, b) E_t

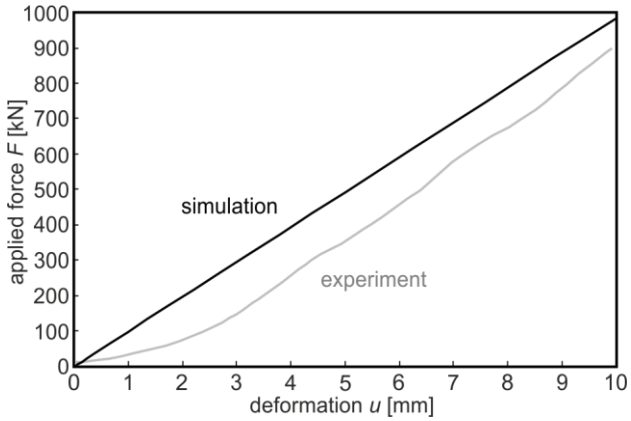

Figure 6: Force-deformation relation of simulation and experiment.

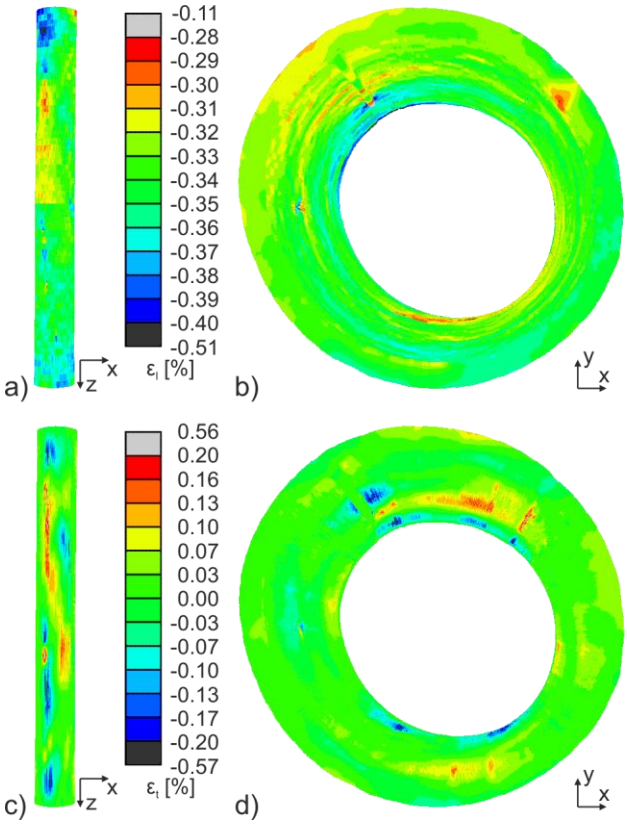

Figure 7: Strain distribution in the finite element model with scattering elastic properties; a) ε_l on surface, b) ε_l at midsection and inside the tube, c) ε_t on surface, d) ε_t at midsection and inside the tube.

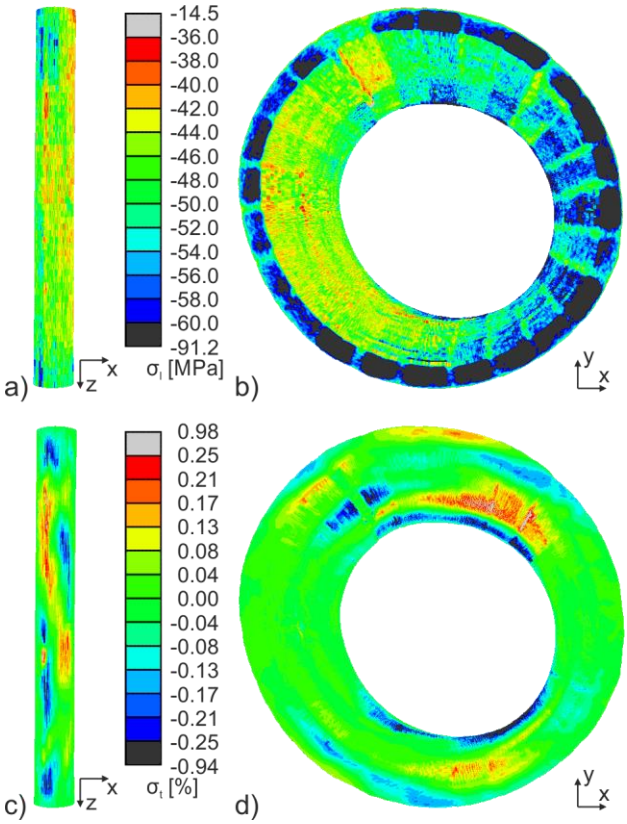

Figure 8: Stress distribution in the finite element model with scattering elastic properties; a) σ_l on surface, b) σ_l at midsection and inside the tube, c) σ_t on surface, d) σ_t at midsection and inside the tube.

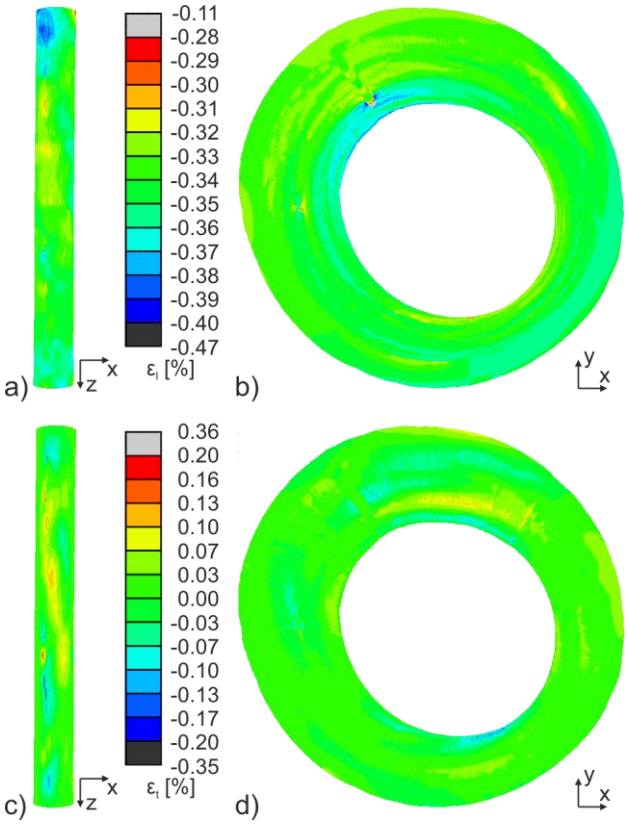

Figure 9: Strain distribution in the finite element model with constant elastic properties; a) ε_l on surface, b) ε_l at midsection and inside the tube, c) ε_t on surface, d) ε_t at midsection and inside the tube.

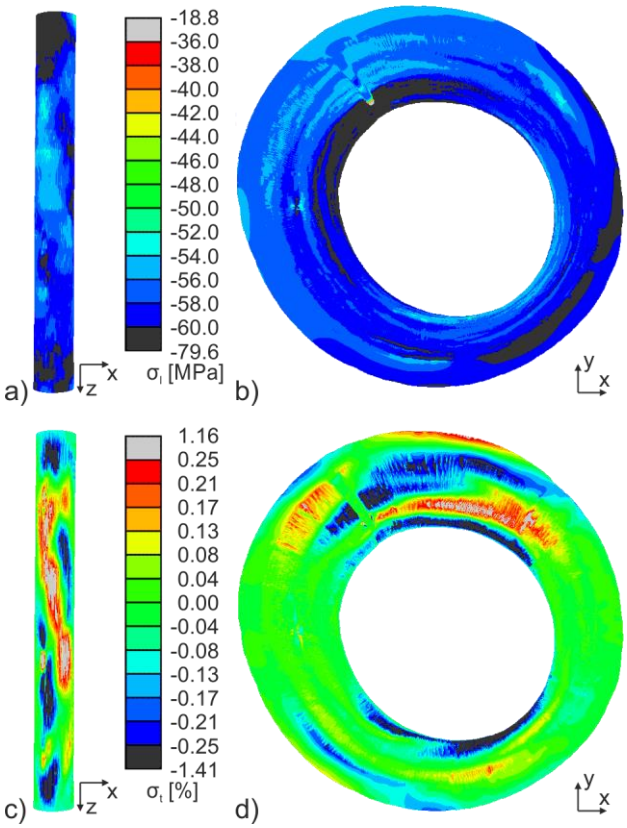

Figure 10: Stress distribution in the finite element model with constant elastic properties; a) σ_l on surface, b) σ_l at midsection and inside the tube, c) σ_t on surface, d) σ_t at midsection and inside the tube.